Correspondence to:

M. D. Pilinski,
Marcin.Pilinski@lasp.colorado.edu

Author Contributions:

Conceptualization: M. D. Pilinski, S. W. Bougher
Formal analysis: M. D. Pilinski, K. J. Roeten
Investigation: M. D. Pilinski, K. J. Roeten, S. W. Bougher, M. Benna
Methodology: M. D. Pilinski, K. J. Roeten
Software: M. D. Pilinski, K. J. Roeten
Supervision: M. D. Pilinski
Validation: S. W. Bougher
Visualization: M. D. Pilinski
Writing – original draft: M. D. Pilinski, K. J. Roeten, S. W. Bougher
Writing – review & editing: M. D. Pilinski, K. J. Roeten, S. W. Bougher, M. Benna

Dynamical Heating in the Martian Thermosphere

M. D. Pilinski[1] , **K. J. Roeten[2]** , **S. W. Bougher[2]** , and **M. Benna[3,4]**

[1]Laboratory for Atmospheric and Space Physics, University of Colorado, Boulder, CO, USA, [2]Department of Climate and Space Sciences and Engineering, University of Michigan, Ann Arbor, MI, USA, [3]Planetary Environments Laboratory, Code 699, NASA Goddard Space Flight Center, Greenbelt, MD, USA, [4]CRESST II, University of Maryland, Baltimore County, Baltimore, MD, USA

Abstract Dynamical heating and cooling are prominent features of planetary atmospheres resulting in thermospheric structures on Venus, Earth and Mars. The purpose of this study is to determine the location and amplitude of localized heating regions in the Martian thermosphere, confirm that they occur in regions of wind convergence and compare the observed dynamical heating with that predicted by a global thermospheric model. This investigation uses several years of data from the NASA Mars Atmosphere and Volatile EvolutioN (MAVEN) mission including observations made by the Neutral Gas and Ion Mass Spectrometer (NGIMS) as well as the Extreme Ultraviolet Monitor (EUVM). Specifically, the analysis focuses on several years of horizontal wind, temperature, and composition data. EUVM measurements provide a solar forcing context for the neutral thermosphere data sets and aid in the statistical analysis. Statistical results are compared with two versions of the Mars Global Ionosphere Thermosphere (M-GITM) global circulation model: one that includes gravity wave parametrization and a version without gravity wave effects. Data analysis indicates that heating features exist around 2–3 and 17–18 local solar time. These locations coincide with regions of converging winds and are in better agreement with M-GITM when a gravity wave parametrization is included in the model. An oscillation in the observed wind field also results in convergence and a density enhancement near 15 local time. While a similar oscillation is reproduced by the model, the amplitude is much lower than observed and may be a result of modeled zonal winds that are too low.

Plain Language Summary The upper reaches of planetary atmospheres act as the interface between the planet and the interplanetary space environment. On Mars, this region is responsible for aerodynamic drag on satellites orbiting the planet. It is also part of the pathway for molecules escaping to space and contributing to the loss of most of the Martian atmosphere and water over the course of billions of years. The motion and structure of the upper atmospheric region are important to understanding and predicting its behavior. We analyzed wind and temperature data collected in the upper atmosphere of Mars by a NASA satellite called the Mars Atmosphere and Volatile EvolutioN spacecraft and compared the results to a model of the Mars atmosphere. The results indicate that locations of converging and diverging winds exist throughout the atmosphere and contribute to its temperature and density structure. These locations of converging winds cause hot spots in the upper atmosphere, particularly on the night side. The wind pattern is also responsible for the presence of large ripples or wave-like features in the dayside atmosphere.

1. Introduction

The global structure of planetary thermospheres can shed light on their energy budgets and transport processes, as well as on the ionospheres to which they couple. Thermospheric structure also affects aerodynamic drag experienced by spacecraft flying at sufficiently low altitudes. This structure is driven by photochemical, radiative, and dynamical processes, as well as by coupling with the lower atmosphere through a variety of mechanisms including gravity waves. The term dynamical heating can refer to adiabatic effects as well as to the deposition of energy by internal gravity waves (as in Hines, 1965). In this paper, the term represents, primarily, the adiabatic heating (and cooling) associated with converging (and diverging) horizontal wind fields. However, there are additional contributions to this source of energy, described in Section 2. The dynamical effects are more difficult to observe and not as well understood. On Earth, dynamical thermospheric effects can cause cooling in the polar thermosphere (Crowley et al., 1995; Schoendorf et al., 1996), for example, while on Venus, night-time heating is associated with adiabatic effects in a region of converging thermospheric winds (Brecht et al., 2011). In fact, this dynamical heating effect is the reason that the night-

side thermosphere can maintain temperatures significantly above absolute zero in spite of the long duration of the Venutian night. On Mars, dynamical effects lead to regions of significant thermospheric temperature and density enhancements, especially near the dawn and dusk terminators (Forbes & Moudden, 2009; Pilinski et al., 2018).

Dynamical processes can lead to both heating and cooling with heating effects being associated with the presence of converging winds. Wind convergence can result from zonal or meridional wind direction reversals or by a rapid slowing of the horizontal winds. This in turn leads to a downwelling in the thermosphere and, often, adiabatic heating.

The presence of dynamical heating regions or thermospheric "heat islands" on Mars was first theorized based on results of global circulation modeling (S. W. Bougher et al., 1990). Pilinski et al. (2018) presented the first empirical evidence for the existence of heat islands using data from the Mars Atmosphere and Volatile Escape (MAVEN) mission (Jakosky et al., 2015).

In this paper, we explore the global structure of thermospheric temperature and winds on Mars to map the location and amplitude of dynamical effects. These properties will also be compared with two versions of a Mars global circulation model, one with and one without a gravity wave parametrization. The sections below describe the theory of dynamical heating and statistical methods used to analyze MAVEN data. This is followed by a description of the global circulation model. Datatypes used in the analysis are then reviewed. Results are presented in three parts: (a) a broad multi-seasonal analysis of winds and temperatures, (b) a statistical analysis focusing on equinox, and (c) an empirical reconstruction of equinox conditions at constant pressure and EUV forcing. Model comparisons are made throughout the results section. Next, we discuss the results in the context of global thermospheric structure and summarize the main conclusions.

2. Dynamical Heating Background

The contribution of dynamical heating to the overall energy budget can be examined through the horizontal and vertical thermodynamic equations as described by Ridley et al. (2006) and adopted here for the Martian thermosphere. The horizontal temperature equation is

$$0 = \frac{\partial \tau}{\partial t} + \frac{u_\phi}{r \cos \theta} \frac{\partial \tau}{\partial \phi} + \frac{u_\theta}{r} \frac{\partial \tau}{\partial \theta} + (\gamma - 1)\tau \left(\frac{1}{r} \frac{\partial u_\theta}{\partial \theta} + \frac{1}{r \cos \theta} \frac{\partial u_\phi}{\partial \phi} - \frac{u_\theta \tan \theta}{r} \right) \tag{1}$$

where the normalized temperature, τ, is defined as

$$\tau = \frac{k_B}{\overline{m}} T \tag{2}$$

where T is the neutral temperature, $\overline{m}$ is the mean molecular mass, k_B is the Boltzmann constant, r is the distance from the center of the planet, θ is the latitude, ϕ is the longitude, u_θ and u_ϕ are the meridional and zonal wind components respectively, and γ is the ratio of specific heats, equal to 5/3. The normalized temperature is equivalent to the total pressure divided by the mass density (Ridley et al., 2006).

The vertical temperature equation is

$$\frac{\partial \tau}{\partial t} + u_r \frac{\partial \tau}{\partial r} + (\gamma - 1)\tau \left(\frac{2u_r}{r} + \frac{\partial u_r}{\partial r} \right) = \frac{k_B}{c_v \rho \overline{m}} Q_{\text{tot}} \tag{3}$$

where u_r is the vertical wind, c_v is the specific heat at constant volume, ρ is the mass density and Q_{tot} is the total energy source term. The specific heat is computed based on the weighted average of the specific heats of individual species weighted by their number densities. Note that the $2u_r/r$ term is due to the divergence of velocities along the radial direction in a spherical coordinate system. The energy source term can be broken down into extreme UV (EUV), infrared (IR), 15 μm (CO_2 LTE and non-LTE terms), and conduction terms as follows

$$Q_{\text{tot}} = Q_{\text{EUV}} + Q_{\text{IR}} + Q_{\text{15um}} + \frac{\partial}{\partial r} \left(\frac{\partial T}{\partial r} (\kappa_C + \kappa_{\text{eddy}}) \right) \tag{4}$$

where κ_C and κ_{eddy} are the molecular and eddy diffusion heat conductivity respectively. These molecular values are calculated based on a mixture of neutral gas contributions (e.g., CO_2, CO, N_2 and O). Details can be found in Bougher, Pawlowski, et al. (2015).

The net dynamical heating, shown below, is the combination of the horizontal hydrodynamic advection (subscript A) and horizontal divergence (subscript B) from Equation 1, as well as vertical hydrodynamic advection (subscript C) and vertical divergence (subscript D) from Equation 3. Horizontal and vertical advection terms (A and C) are proportional to the product of their respective wind components and the corresponding component of the temperature gradient. The divergence terms (B and D) are proportional to the spatial gradients of the wind components. Terms A and B, horizontal advection and divergence, make up the largest contributions to the dynamical heating term. We would therefore expect the possibility of strong dynamical heating in locations of large horizontal wind magnitudes *and* strong horizontal thermal gradients as well as locations of large wind changes (magnitude and/or direction). M-GITM solves Equation 1, the left side of Equation 3, and the source terms on the right side of Equation 3 independently and the resulting dynamical heating terms can be isolated in post-processing.

$$Q_{\text{TDYN}} \overset{\text{def}}{=} \left[\frac{u_\phi}{r\cos\theta} \frac{\partial\tau}{\partial\phi} + \frac{u_\theta}{r} \frac{\partial\tau}{\partial\theta} \right]_A + \left[(\gamma-1)\tau \left(\frac{1}{r} \frac{\partial u_\theta}{\partial\theta} + \frac{1}{r\cos\theta} \frac{\partial u_\phi}{\partial\phi} \right) \right]_B$$
$$+ \left[u_r \frac{\partial\tau}{\partial r} \right]_C + \left[(\gamma-1)\tau \left(\frac{2u_r}{r} + \frac{\partial u_r}{\partial r} \right) \right]_D$$

(5)

Vertical neutral winds are not measured by MAVEN and therefore, the vertical terms C and D will be omitted when analyzing observed wind statistics using Equation 5. Based on a model evaluation (see Section 3), the error caused by not including vertical winds is not expected to change the overall diurnal pattern of dynamical heating.

3. Methods

3.1. Statistical Analysis of Temperatures and Neutral Densities

Observations of Argon densities made by NGIMS are converted to neutral temperatures (T_n) using the approach described by Snowden et al. (2013) and used previously by Pilinski et al. (2018). These temperatures are combined with neutral observations of CO_2 and atomic oxygen (O) number densities to compute a neutral pressure at each satellite location. Neutral temperatures are analyzed for both the descending and ascending portions of the MAVEN orbit due to the rapid nature of Argon transmission through the NGIMS inlet. Neutral densities and pressures are analyzed only on the descending (inbound) segments of each orbit as the outbound CO_2 and O data is distorted by the buildup of these molecules on the instrument walls.

Several types of statistical analysis are performed using the resulting temperatures and pressures. The first is a straightforward binning of existing temperature and wind data in season, local time, latitude, and altitude. Unless otherwise noted, bins are 20 km wide in altitude, 30° wide in latitude, and 3 hr wide in local solar time (LST). Note that this altitude analysis is performed above 150 km altitude where, according to the M-GITM model, the dayside vertical gradients of temperatures and winds are expected to be <15K and <10 m/s respectively over an altitude change of 20 km. While the number density scale heights are generally less than the bin altitude (10–15 km), number densities will not be binned.

A variation of this binning is performed for the horizontal wind data in season (L_s angle), latitude, and local time only. This is because horizontal winds are not expected to significantly vary with altitude due to the high viscosity of the thermosphere in this region. Note that the majority of the wind measurements were collected above 140 km altitude with the average minimum altitude of wind measurements being above 150 km. The M-GITM model predicts that the change in wind component magnitudes due to any vertical gradients should be negligible (<10 m/s). During equinox, the modeled wind pattern is approximately symmetric about the equator, particularly at low to mid latitudes. As will be shown later, this is mostly true for the observed winds as well. Since wind data are collected in intermittent campaigns lasting several days, taking advantage of this symmetry allows for more complete coverage of the hemispheric wind pattern than would otherwise be possible. The meridional winds in this case are converted into equatorward/anti-equatorward directions and, along with the zonal component, are reflected around the equator. Since aggregating data for equinox conditions include a broad swath of L_s angles, it is possible that the line of symmetry will depart slightly from the ideal of 0° latitude in IAU coordinates. Therefore, we perform data binning Mars-sun-orbit (MSO) coordinates in order to at least partially compensate for this effect. The
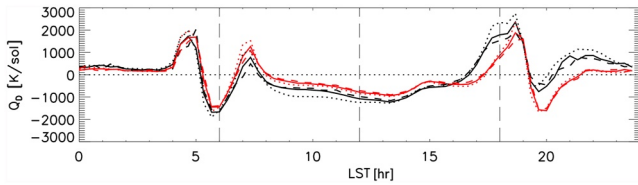
Figure 1. Dynamical heating computed using M-GITM_{GW} winds and temperatures at three different pressure levels in the thermosphere. The black lines represent dynamical heating using both horizontal and vertical advection and divergence terms. The red lines represent the dynamical heating computed using only the horizontal terms.

"equator" in MSO coordinates follows the subsolar point, which is the location of peak solar heating and orients the diurnal wind pattern. We confirmed this symmetry by comparing the M-GITM winds in MSO coordinates at 200 km at various L_s angles. Once the equinoctial wind statistics are compiled, a series of Fourier curve fits to the low-mid latitude meridional and zonal wind components is used to compute an approximate low/mid-latitude wind-field divergence. The resulting average wind field is used to estimate divergence and to compute the dynamical heating based on Equation 5. Neglecting the vertical components is not expected to change the sign of the QD term nor the location of its peaks by more than 1 hr of local time. To confirm this, a similar analysis is performed using model winds and temperatures from M-GITM_{GW}. Figure 1 shows the dynamical heating term at three pressure levels using all terms of Equation 5 (black) and using only the horizontal terms (red). The pressure levels shown are 5.4×10^{-6} Pa (dashed), 1.3×10^{-6} Pa (solid), and 3.4×10^{-7} Pa (dotted). These pressure levels correspond to daytime altitudes of approximately 150, 165, and 185 km, respectively.

Figure 1 demonstrates that omitting the vertical winds, while not inconsequential, still provides a reasonable representation of the dynamical heating (QD) with the location of heating and cooling peaks being the same within 0.5 hr of local time in both cases. The qualitative nature of the QD diurnal structure is also well represented.

The Mars thermosphere is highly variable at multiple temporal and spatial scales ranging from gravity waves (GW) and tides (Bougher, Brain, et al., 2017; Bougher, Cravens, et al., 2015; England et al., 2017; Medvedev et al., 2011; Thaller et al., 2021) to EUV driven variability over the solar cycle (Thiemann et al., 2018) and due to the Mars orbital position transitioning from perihelion to aphelion. Furthermore, steep density gradients exist (Pilinski et al., 2018) across the terminator. Characterizing the spatial variability of the thermosphere observed from a satellite in a processing elliptical orbit is therefore challenging due to the potential for aliasing the various sources of spatial and temporal variability. To reduce the potential for aliasing, low-to-mid latitude neutral temperatures will be divided into local time and pressure level bins. Each bin will include several days of data to reduce any GW and nonmigrating tide contribution in the binned results. The neutral temperature response to EUV heating within each bin can then be analyzed and controlled. The Lyman alpha channel of the EUVM instrument (Eparvier et al., 2015) serves as a proxy for EUV heating. For bins that contain sufficiently diverse EUV sampling (spanning at least 0.005 W/m²), a linear fit is used to record the EUV-T_n relationship. To evaluate changes in the potential energy (vertical movement of pressure levels), the pressure-level altitude (P_{height}) is fitted using both linear and nonlinear fits. The nonlinear fit represents the diminishing increase in P_{height} at higher EUV but requires that the data in the bin include EUV values high enough to be meaningful. Organizing the data by pressure-level also allows any spatial differences in sampling within each bin to be reduced, as does the $\pm 50°$ degree MSO cutoff. In the last stage of our analysis, limiting the data set to L_s angles of $-45°$–$45°$ and $135°$–$225°$ (vernal and autumnal equinoxes combined) limits the seasonal variability within the data set and enables the assumption of approximate hemispheric symmetry. The resulting set of linear and nonlinear fits for each pressure level and local time constitute a simple empirical T_n model that can represent the diurnal configuration of the low-latitude equinox thermosphere by interpolating to a fixed EUV irradiance.

3.2. M-GITM

3.2.1. Standard M-GITM Implementation

The Mars Global Ionosphere Thermosphere Model (M-GITM) combines the Earth GITM source code (e.g., Ridley et al., 2006) with physical parameters appropriate for the Mars atmosphere, key radiative processes, and ion-neutral chemistry, to capture the main features of the Mars atmosphere spanning altitudes from the surface to approximately 250 km (e.g., Bougher, Pawlowski, et al., 2015). M-GITM is normally configured with a 2.5 km vertical resolution, $5 \times 5°$ horizontal resolution, and a ~2-s time step. Model physics and simulated features directly benefit from the lower to upper atmosphere coupling made possible with this whole atmosphere framework.

M-GITM simulates the coupled thermal, dynamical and chemical drivers (Bougher, Pawlowski, et al., 2015). For the lower atmosphere (~0–80 km), a correlated-k radiation code was adapted from the NASA Ames Mars General Circulation Model (MGCM) (Haberle et al., 1999). This code simulates the long and short wavelength

solar heat inputs, heating associated with aerosol absorption (seasonally variable), and CO_2 15-μm cooling below ~80 km (where the atmosphere is local thermal equilibrium, or LTE). Dust opacity distributions are based on maps of empirical dust opacity spanning several Martian years (e.g., Smith, 2004, 2009).

Important boundary conditions include those at the top of the model (near the exobase) and at the surface. Topside conditions allow vertical density gradients to be continuous, consistent with molecular diffusion. When coupled with a zero gradient in vertical velocities, a non-zero flux boundary condition is maintained. Furthermore, topside temperatures are specified to be isothermal, consistent with the exobase approximation. At the surface, densities are specified from empirical estimations, along with temperatures for which observed diurnal and seasonal variations are prescribed. In addition, surface thermal inertia and albedo are prescribed in accord with 2-D maps from the NASA ARC model (e.g., Haberle et al., 2003). Further description of the M-GITM lower boundary conditions can be found in the literature (Bougher, Pawlowski, et al., 2015).

For the upper atmosphere (~80–250 km), a CO_2 non-LTE 15-μm cooling approach was added (González-Galindo et al., 2013), enabling interactive CO_2 cooling to be simulated as atomic O abundances vary. M-GITM utilizes daily Flare Irradiance Spectral Model for Mars (FISM-M) outputs based on EUV and UV fluxes collected by the MAVEN Extreme Ultraviolet Monitor (EUVM) (Thiemann et al., 2017). The thermospheric heating as well as dissociation and ionization rates are then simulated at each model time step (Bougher, Pawlowski, et al., 2015).

Values of neutral temperatures, neutral and ion number densities (CO_2, CO, N_2, O, O_2, He, Ar, N^4S, CO_2^+, O_2^+, O^+, NO^+. N_2^+) along with the three components of the neutral wind vector are output on a regular three-dimensional grid. In this analysis M-GITM was run for the aphelion, autumnal equinox, and perihelion seasons for conditions corresponding to MY33 (Ls = 90°, 180° and 270°).

Past comparisons of M-GITM simulations with measurements include sampling consistent with the six MAVEN Deep Dip campaigns (Bougher, Jakosky, et al., 2015; Zurek et al., 2017) and science orbits with periapses in the dayside of the thermosphere (Bougher, Roeten, et al., 2017). The M-GITM code has been validated against in-situ and remote-sensing measurements from the MAVEN Accelerometer (ACC), NGIMS, and Imaging Ultraviolet Spectrograph (IUVS). For example, dayside (SZA <60°) NGIMS densities and extracted temperatures were compared with corresponding M-GITM fields along Deep Dip two orbit trajectories (Bougher, Jakosky, et al., 2015). These comparisons revealed that M-GITM dayside temperatures closely match NGIMS derived temperatures at low SZA. M-GITM also produced significant dynamical heating and warm temperature bulges at the evening terminator that were subsequently discovered in NGIMS data sets (Pilinski et al., 2018). By contrast, the maintenance of the nightside density and temperature structure is still poorly understood (Zurek et al., 2017). A version of M-GITM addressing gravity wave effects has been developed by Roeten et al. (2022), and is also reviewed briefly at the end of this section.

The significant evening terminator heat island features in the Martian thermosphere have been predicted by various three-dimensional global circulation models (GCMs) prior to the MAVEN mission and NGIMS measurements (above). The coupled NASA Ames Mars Global Circulation Model (MGCM)- NCAR Mars Thermospheric General Circulation Model (MTGCM) framework initially predicted strong evening terminator heat island features, especially at Equinox and Perihelion seasonal conditions at low to mid-latitudes (e.g., Bougher et al., 2008; Valeille et al., 2009). In addition, a comparison study investigated temperature and wind features simulated by the MGCM-MTGCM and the LMD-MGCM codes for common input conditions (González-Galindo et al., 2010). Both models produced strong dynamical heating at the evening terminator, giving rise to significant warming (in excess of ~30–50°K over what was otherwise expected). Weaker morning terminator warming was also revealed by each model. Two model dynamical terms were compared to confirm the sources of this heating. Finally, strong evening terminator dynamical heating was simulated for Aphelion, Equinox and Perihelion seasonal conditions by initial M-GITM simulations prior to MAVEN (Bougher, Pawlowski, et al., 2015). All subsequent M-GITM simulations have reproduced similar strong evening terminator heat island features.

Post-processing tools are typically used to visualize heat balance terms extracted from the M-GITM code thermal equation sources during model runtime. A separate history file is assembled to contain radiative and dynamical terms taken from the code at 1-hr intervals throughout a given simulation. These terms include (a) EUV and UV heating rate, (b) NLTE CO_2 15-μm cooling rate, (c) molecular and eddy thermal conduction, (d) LTE and NLTE near-IR heating rate, and (e) dynamical heating/cooling terms. For the latter, a combination of four dynamical terms gives rise to the net dynamical heating rate: (a) horizontal hydrodynamic advection, (b) vertical

hydrodynamic advection, (c) horizontal divergence, and (d) vertical divergence. Two of these terms (vertical advection and vertical divergence) are new to the M-GITM 5-moment equation formulation, since the vertical momentum equation is solved explicitly in the GITM framework. This means that the M-GITM solves the vertical and horizontal momentum equations separately. Ultimately, vertical profiles of heating/cooling terms are combined into single location (latitude/local time) plots for easy display of the diurnally reproducible balances of these terms giving rise to the corresponding vertical temperature profile. For M-GITM simulations, diurnally reproducible conditions are achieved as "spin-up" of the model occurs, for which primary fields converge to nearly constant values (within a tolerance). This is achieved after roughly 20 Martian solar days (sols) of integration, and the initial conditions no longer have an impact on the simulated fields. The initialization is always the same: globally uniform 1-D density and temperature profiles with zero horizontal and vertical wind magnitudes. Heat balance terms also have diurnally reproducible values corresponding to the temperatures. Lastly, this integration time is selected for all model simulations conducted. Such a stabilization is required before proceeding to extract model fields for analysis.

Note that while the GITM models are capable of reproducing conditions associated with non-hydrostatic equilibrium, such effects were shown to be relevant for brief times during large increases in thermospheric energy inputs (Deng et al., 2008). The conditions explored in this paper do not include such disturbances and instead focus on diurnally reproducible climatological states of the global circulation pattern achieved using constant energy inputs. These diurnally reproducible states represent a thermosphere that is in hydrostatic equilibrium.

3.2.2. M-GITM With a Gravity Wave Parametrization Scheme

A nonlinear and non-orographic gravity wave (GW) parameterization scheme was incorporated globally in M-GITM in order to account for the effects of gravity waves in the Martian thermosphere. Throughout this paper, we will refer to this version of the model as M-GITM$_{GW}$. Results from new M-GITM$_{GW}$ simulations which include this GW scheme indicate that the effects of GWs can be significant in the upper atmosphere, impacting wind speeds as well as the temperature structure at these altitudes (Roeten et al., 2022).

These changes occur since the scheme allows M-GITM$_{GW}$ to account for both momentum deposited by GWs as well as heating directly produced by wave dissipation and heating/cooling corresponding to the divergence of wave-induced heat flux. Indirect changes to dynamical heating can also result from changes in wind speed and the general circulation with the addition of the GW drag in the forcing terms. It follows that an impact on the simulated dynamical heat island features near the terminators might also be expected. To test this, new M-GITM$_{GW}$ simulations run over the same time period were completed. Except for the addition of the GW scheme, all other key parameters used in the M-GITM simulations were unchanged.

The GW scheme used in M-GITM$_{GW}$ was originally designed for Earth's upper atmosphere (Yiğit et al., 2008) and has since been modified for use in Mars GCMS (Medvedev et al., 2015; Medvedev & Yiğit, 2012). It is specifically prescribed for the effects of non-orographic GWs, includes nonlinear interactions between harmonics, and is appropriate for wave propagation and dissipation in the Martian upper atmosphere. The parameterization in the model calculates the evolution of a spectrum of GWs as they propagate upward from a source level in the lower atmosphere. The specified GW spectrum is an empirical Gaussian distribution that has been used previously in Earth and Mars GCMs, defined in terms of maximum horizontal momentum fluxes at the source altitude as a function of horizontal phase speeds. For the simulations run here, a source flux of 0.0025 m^2/s^2 was used with a maximum phase speed of ±80 m/s, and a source height of ~9 km. A 300 km horizontal wavelength is used and is consistent with previous findings (Creasey et al., 2006; Siddle et al., 2019; Terada et al., 2017, assuming that the wave structures observed in the Mars thermosphere were due to horizontal variations). A more detailed description of the GW scheme currently being used in M-GITM can be found in Roeten et al. (2022), and the references therein.

4. Data

The MAVEN spacecraft was launched on 18 November 2013 on a mission to explore the loss of the Martian atmosphere to space. It arrived at Mars on 21 September 2014 and began science operations in October 2014. The MAVEN spacecraft is nominally in an elliptical, 150 km × 6,000 km, orbit with a 4.5-hr period and an inclination of 75° with respect to the Martian equator. Since August 2020, the MAVEN periapsis is kept closer to 200 km altitude. MAVEN carries a number of neutral and plasma instruments to characterize the ionosphere, solar wind,

neutral atmosphere, magnetic field, and solar EUV forcing. An in-depth review of MAVEN and its mission is provided by Jakosky et al. (2015). In this work, we analyze MAVEN Neutral Gas and Ion Spectrometer (NGIMS) data collected from October 2014 through August 2020. The Mars thermosphere is heated by solar extreme ultraviolet irradiance and we use data from the Extreme Ultra-Violet Monitor (EUVM) on MAVEN to organize some of the analysis described below.

4.1. Neutral Density and Temperature Data

Neutral densities and composition are measured by the Neutral Gas and Ion Mass Spectrometer (NGIMS), which is described in detail by Mahaffy et al. (2015). Neutral density measurements can be used to compute neutral temperature and pressure, as described in a previous section. In this paper, we use the closed source neutral mode of NGIMS as it has a higher signal-to-noise ratio. Non-volatile species such as atomic oxygen and CO_2 tend to undergo reactions on the surfaces of the accommodation chamber and transfer tube. The effects of these reactions are most prominent during the ascending pass of each orbit where the increased "ram pressure" at periapsis leads to large values of surface coverage for non-volatile species. For this reason, we only use closed source measurements of O and CO_2 on the descending sides of each MAVEN orbit.

NGIMS measurements of Argon density are converted to neutral temperature. Neutral temperature calculations use the method described by Snowden et al. (2013), which assumes hydrostatic equilibrium and integrates along the Argon density-altitude profiles. Argon measurements were been shown to have a sufficient signal-to-noise ratio for this method to be applied in the region of interest (Stone et al., 2018).

Estimates of neutral temperature and the number densities of the primary neutral species (CO_2 and O) are combined to compute neutral pressure.

$$P = k_B(n_{44} + n_{16})T_n \tag{6}$$

The density data corresponds to version 01 and revision 02 (v01_r02) of the NGIMS L1b data products found on the NASA PDS server.

4.2. Wind Data

In addition to sampling neutral and ion species to determine the composition of the Martian upper atmosphere, the NGIMS instrument has another mode of operation that allows it to measure in situ thermospheric horizontal neutral wind velocities. During this mode, NGIMS' typical data collection is paused as the instrument platform sweeps back and forth by $\pm 8°$ across the spacecraft ram direction. Wind velocities are then extracted from the modulations observed in the neutral and ion fluxes as the pointing direction of the instrument varies. The technique by which NGIMS measures wind velocities is described in detail in Benna et al. (2019).

Wind measurements take place along the spacecraft's track through the thermosphere at altitudes ranging from ∼140 to 220 km. This measurement technique assumes that vertical winds are negligible, which is believed to be a reasonable assumption for typical driving conditions (Bougher, Pawlowski, et al., 2015). It is also assumed that winds do not vary significantly within the 30 s it takes for the instrument to complete a full motion cycle. Uncertainties in the measurements are primarily due to potential errors in the reconstructed ephemeris of the spacecraft trajectory and direction of the NGIMS boresight, due to the energy resolution of the mass filter in the instrument and counting statistics (Benna et al., 2019). Uncertainties typical of the along- and across-track wind magnitudes are 20 and 6 m/s, respectively (Benna et al., 2019).

Wind observations most commonly take place within campaigns occurring over 2–3 days every month. Within a campaign, 5–10 consecutive orbits of neutral wind measurements are taken. Due to the nature of MAVEN's orbit, during an individual campaign, each orbit of wind observations tracks along nearly the same local times, latitudes, and altitudes, but different longitudes. Note that the maximum aerographic latitude MAVEN flies over is 75°.

This analysis relies on neutral wind data collected between March 2016 and April 2021. During this period, campaigns typically occurred at least once a month, with a few exceptions of larger gaps between campaigns (i.e., gaps October–December 2016 and February–April 2019). The neutral winds data set used is a NGIMS Level 3 data product (v03_r01).
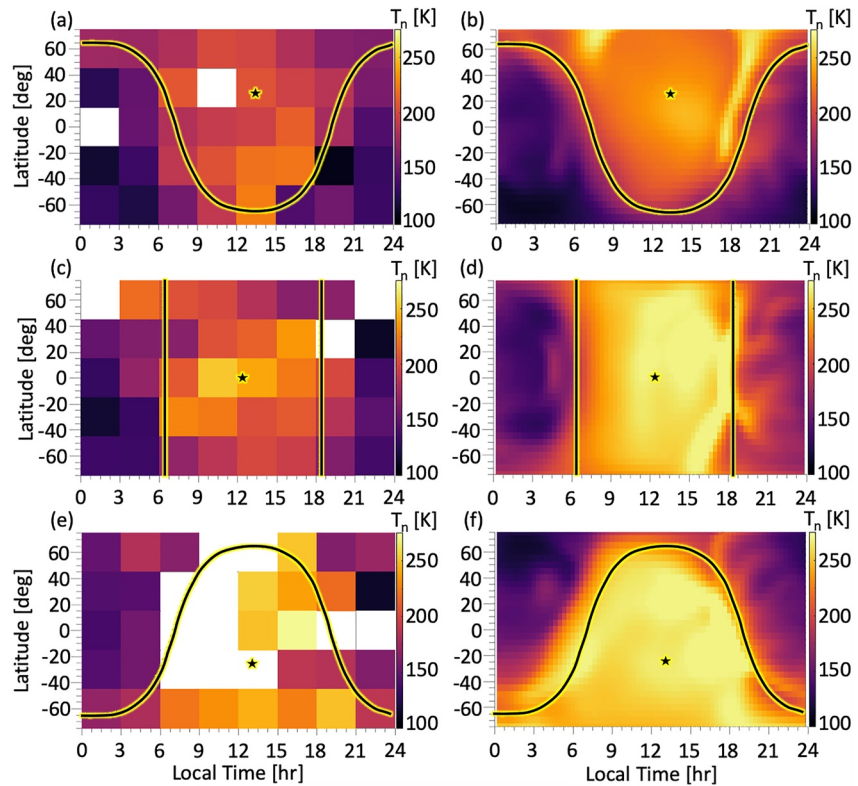
Figure 2. Seasonal statistical analysis of observed (left) and M-GITM (right) temperatures at 165 km altitude. The seasons are aphelion (a, b) Ls 220–320, equinox (c, d), and perihelion (e, f) or Ls 40–140. The white boxes indicate a lack of sufficient data for a statistical analysis.

4.3. EUV Irradiance Data

Irradiance observations are obtained from MAVEN Extreme UltraViolet Monitor (EUVM) (Eparvier et al., 2015). The EUVM data set nominally provides solar irradiance once per orbit in three spectral bands including the Lyman-alpha and 17–22 nm bands. In this work, we use Lyman-alpha measurements from version 13, revision 1 of the level 2b EUVM product (v13_r01). This irradiance product is provided once per orbit and is interpolated to the time of interest.

5. Results

5.1. Statistical Results Based on Season

Seasonal statistics for the median observed and M-GITM (without GW parametrization) temperatures at 165 km are presented in Figure 2 for aphelion (northern summer), equinox, and perihelion (southern summer) conditions in the top, middle, and bottom panels respectively. Note that data from both autumnal and vernal equinoxes are combined in panel 2c. The left panels (a, c, e) are based on a simple binning of the MAVEN data without controlling for EUV conditions. The right hand panels (b, d, f) are M-GITM results at the equivalent altitude and season. Black and yellow lines indicate the location of the terminator at 165 km altitude while the star is the location of the subsolar point. Starting with aphelion, we note that the warmest global temperatures occur away from the subsolar point in the winter (southern) hemisphere in the observations (panel a). The model indicates temperature maxima along the dusk and dawn sectors at high latitudes, with the dusk peak-temperature feature also extending along the terminator and into the winter hemisphere. The statistical results (2a) are qualitatively similar with the M-GITM temperature distribution in Figure 2b. As we will show later, the aphelion distribution of peak temperatures can be explained well by dynamical heating in regions of converging thermospheric winds. The equinox comparison between data (2c) and model (2d) confirms warm temperatures near the subsolar point, but the pre-dusk terminator feature that is so prominent in M-GITM results at 17–18 LST is difficult to see in the
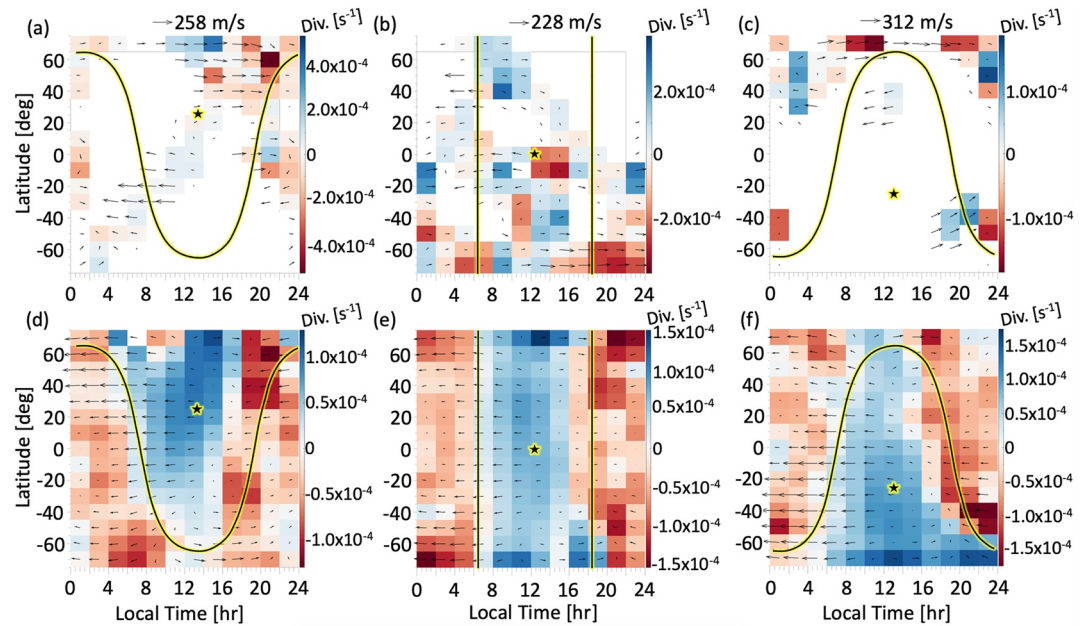
Figure 3. Statistical (top) and M-GITM (bottom) winds. Color maps represent the divergence of the wind field in units of s^{-1}. Results are shown for aphelion (a, d), equinox (b, e), and perihelion (c, f). Black and yellow lines indicate the location of the terminator, while the star in each panel is the location of the subsolar point.

statistics. Nevertheless, the statistical results at ±30° latitude do indicate a temperature increase that occurs prior to 18 LST. The diminished amplitude of the observed feature may be a result of the low spatial resolution of the bins but may also be due to other sources of variability introduced into the statistics. For example, the equinox sampling incorporates a wider range of EUV forcing conditions than the other seasons sampled in Figure 2. These EUV conditions are not always represented equally in each bin. Meanwhile, each model result in panels (b, d, f) corresponds to a single EUV irradiance value. Perihelion results appear in Figures 2e and 2f. The incomplete data coverage during this season means that temperature statistics are not available in the entire dayside. The available data do indicate temperature enhancements just prior to the dusk terminator, especially near the equator. A temperature enhancement in the summer hemisphere (southern latitudes) prior to the dusk terminator is also apparent in Figure 2e. These observed perihelion features agree qualitatively with the M-GITM temperature structure near dusk in Figure 2f.

Next, we examine the observed statistical winds and compare them with M-GITM simulated winds. The observed and modeled divergence of the horizontal wind field is computed using term B in Equation 5. Figure 3 displays the statistical (panels a, b, c) and M-GITM wind fields (panels d, e, f) where the vector plots indicate the average wind direction and magnitude, while the color maps indicate divergence (blue for positive divergence associated with dynamical cooling and red for negative divergence associated with dynamical heating). Three seasons are represented in Figure 3: aphelion (a, d), equinox (b, e), and perihelion (c, f). As before, the season-averaged terminator location is indicated by crosses while the subsolar point is indicated by an asterisk in each panel.

At aphelion, the observed (3a) low latitude winds generally exhibit zonal divergence (blue) on the dayside and convergence (red) just past the dusk terminator and also around midnight. Convergence values are also high in the dayside summer hemisphere (north) especially near the terminator. The M-GITM results for aphelion (3d) are qualitatively consistent with the statistical winds in that convergence peaks around summer dayside hemisphere near the dusk terminator with moderate convergence around the low latitude dusk terminator. The location of zonal wind reversal and convergence in the nightside winter hemisphere occurs near midnight in the M-GITM results, but in the statistical results zonal convergence can be inferred to occur in the early morning (see wind directions prior to dawn terminator southern hemisphere in panel a). The near equatorial dusk temperature enhancement in Figure 2a is located near the converging winds observed in the vicinity of the dusk terminator. Unfortunately, the statistically observed temperature enhancements in the southern hemisphere (Figure 2a) lack corresponding spatial coverage in terms of wind observations (Figure 3a). Also, the strong convergence around

the summer hemisphere dusk terminator has no corresponding temperature enhancement in Figure 2a. This could again be due to the coarse resolution of the temperature analysis however.

A notable feature of the low latitude equinox winds is a region of convergence around 12–16 LST rather close to the subsolar point (Figure 3b). This region of convergence is caused primarily by equatorward meridional winds on both North and South sides of the low-latitude region. Examining the region south of the dayside equator, the equatorward winds near 15 LST are part of a rotation pattern centered approximately at 30° south latitude and 12 LST. It seems reasonable that this would be the case in the northern hemisphere as well although data coverage in this region is incomplete. There is no equivalent dayside convergence feature in the equinox modeled thermosphere near the subsolar point (Figure 3e) but there is a larger rotation pattern centered ±40° latitude and 15 LST which turns the modeled mid-latitude winds equatorward starting around 17 LST and culminating in the modeled peaks in convergence at 18–19 LST. The statistical dayside equatorward winds originate from more than one wind campaign and cannot readily be ascribed to an anomalous time period or atmospheric condition (e.g., EUV irradiance or dust storm for example). As with aphelion, low latitude zonal convergence (zonal wind reversal) occurs post-midnight (3 LST) at equinox in the statistical results, and pre-midnight (18–19 LST) in the M-GITM outputs. Where data are available, high convergence values are observed near the terminators, which is consistent with model results. The equinox M-GITM results indicate that mid-to low-latitude winds and convergences are approximately symmetric about the equator.

Perihelion statistical winds have the sparsest coverage of the three seasons. Nevertheless, strong convergence values are seen near the terminator and midnight in the summer hemisphere (south) in both the statistical and M-GITM results. As with aphelion and equinox, there is some evidence that zonal wind reversal does not occur pre-midnight (in the summer hemisphere for example) with eastward winds dominating across the terminator into later local times in the observed statistics for the southern hemisphere (3c) while the M-GITM winds indicate a reversal around the same location. The sparsity of the perihelion wind statistics makes it difficult to correlate temperature enhancements in Figure 2e with statistical winds in Figure 3c.

The range of divergence values across the three seasons based on the statistical analysis is larger than those estimated from model winds. The largest data-model difference in divergence magnitudes occurs at aphelion. This is in spite of the wind magnitudes being comparable between the statistical and model results. Statistical divergence magnitudes also seem to increase from perihelion (3c) to aphelion (3a), a trend that is not present in the M-GITM results. When comparing divergence values in the high latitude dusk-side summer regions, the divergence peaks at $\sim$0.0005 s^{-1} at aphelion (3a), 0.0003 s^{-1} at equinox (3b), and 0.00015 s^{-1} at perihelion (3c). This would signify that as the solar EUV irradiance decreases at higher Mars-Sun distances, the dynamical heating/cooling increases, reinforcing its relative contribution to the thermal state of the thermosphere.

Another way in which the standard M-GITM runs disagree with observed wind statistics is that at mid to high latitudes (beyond $\sim$50° north or south latitude), there is an absence of observed reversal in the zonal winds. This is most clearly seen in the northern aphelion hemisphere in panel a, southern equinox hemisphere in panel b, and northern perihelion hemisphere in panel c where, for all seasons, the observed polar rotation is predominately eastward. In other words, observed winds provide evidence of an eastward neutral wind jet above 50° latitude. Meanwhile, the M-GITM zonal reversal can be seen in the model results around 12 LST along with a corresponding increase in divergence at all seasons.

The results shown above indicate that regions of enhanced thermospheric temperatures often occur away from the subsolar point at locations of converging winds (e.g., Figures 2a and 3a). Such temperature enhancements are well represented by the M-GITM model. Furthermore, observed winds confirm that significant convergence can exist near the equator, an important ingredient for dynamical heating. Significant nighttime convergence is predicted by this M-GITM version and occurs in the pre-midnight local times. In contrast, the observed nighttime convergence occurs in the post-midnight region. Most surprising is a region of dayside equatorial convergence observed at equinox. This feature is associated with converging meridional winds and does not appear in the M-GITM results. Further analysis is needed to determine if this feature is observationally and statistically robust.

5.2. Equinox Empirical Reconstruction at Constant Solar Irradiance

To alleviate some of the challenges associated with data sparsity and binning resolution when evaluating the wind field and convergence is taking advantage of the approximate hemispheric symmetry in the equinox circulation.
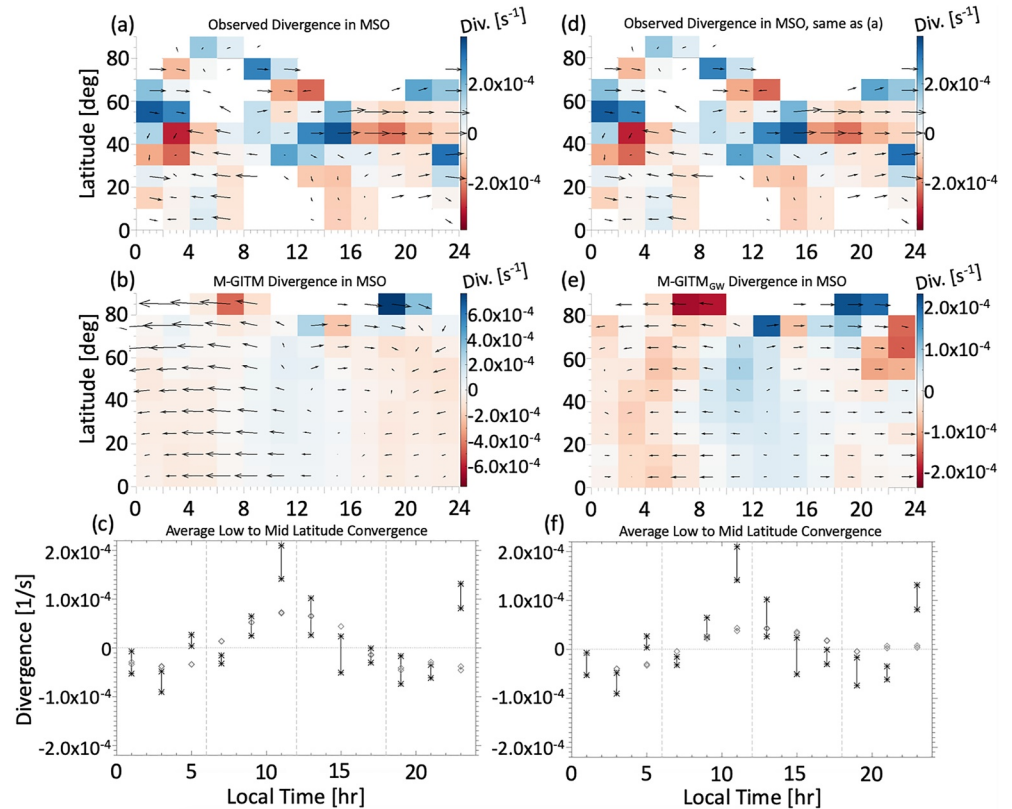
Figure 4. Equinox winds plotted in MSO coordinates assuming wind-field symmetry around the equator. The colormap indicates the value of divergence. Panels (a, d) are the observed equinox winds and are repeated at the top to aid in comparison with the plots below, panel (b) shows the M-GITM results without gravity wave effects, panel (e) shows model winds from a version of M-GITM$_{GW}$ that includes gravity waves, and panels (c, f) indicate the low to mid-latitude averaged divergence computed using modeled (diamonds) and measured (asterisk) winds. The range of values indicated in panels (c, f) for both the model and measured divergence illustrates the difference between taking the average divergence between 0°–50° latitude and 0°–40° latitude. Panel (e) M-GITM results do not include gravity wave effects and panel (f) M-GITM$_{GW}$ results include gravity wave effects. Note that the divergence color scales are not the same in each of the panels.

First, we use MSO coordinates to reduce any meridional shifts in the circulation pattern within a limited set of solar longitudes (L_s). The meridional wind component is then converted into equatorward and anti-equatorward directions such that data from the north and south hemispheres can be combined. High and very low EUV values are also excluded from the analysis resulting in EUV conditions between 0.0025 and 0.0032 Wm^{-2}. The results of this analysis can be seen in Figure 4. The main equinox features described in the IAU wind statistics (Figure 3) are also present in Figures 4a/4d including the low latitude meridional convergence around 15 LST and the zonal convergence occurring post-midnight at approximately 2–3 LST. The M-GITM wind fields are analyzed in the same way and the results shown in Figure 4b for a version of M-GITM without GW effects. Note that the color-scale between panels a/d, b, and e is different. Figure 4c shows the average low-latitude divergence from the equator to 40° and 50° MSO latitudes, as indicated by two values shown at each local time. The range of statistical convergence (asterisk values connected by a line) is compared to the equivalent M-GITM analysis (diamonds). The modeled and observed horizontal divergence share the same approximate diurnal structure, with predominately divergent flow on the dayside and convergent flow on the nightside. Differences include a larger observed pre-midnight divergence and larger observed post-midnight convergence as well as the aforementioned observed convergence around 15 LST. Another feature of the observed convergence is a wave-like behavior with a 4-hr LST wavelength (3,500 km) in some local time ranges, primarily 0–10 LST and 12–20 LST.

The right side of Figure 4 contains the same analysis of observed winds (4d) along with the analogous model results from M-GITM$_{GW}$ in panel 4e and the average low-latitude divergence based on data and M-GITM$_{GW}$. The inclusion of GW wave effects removes the rotation pattern seen in the afternoon and centered on 16 LST in
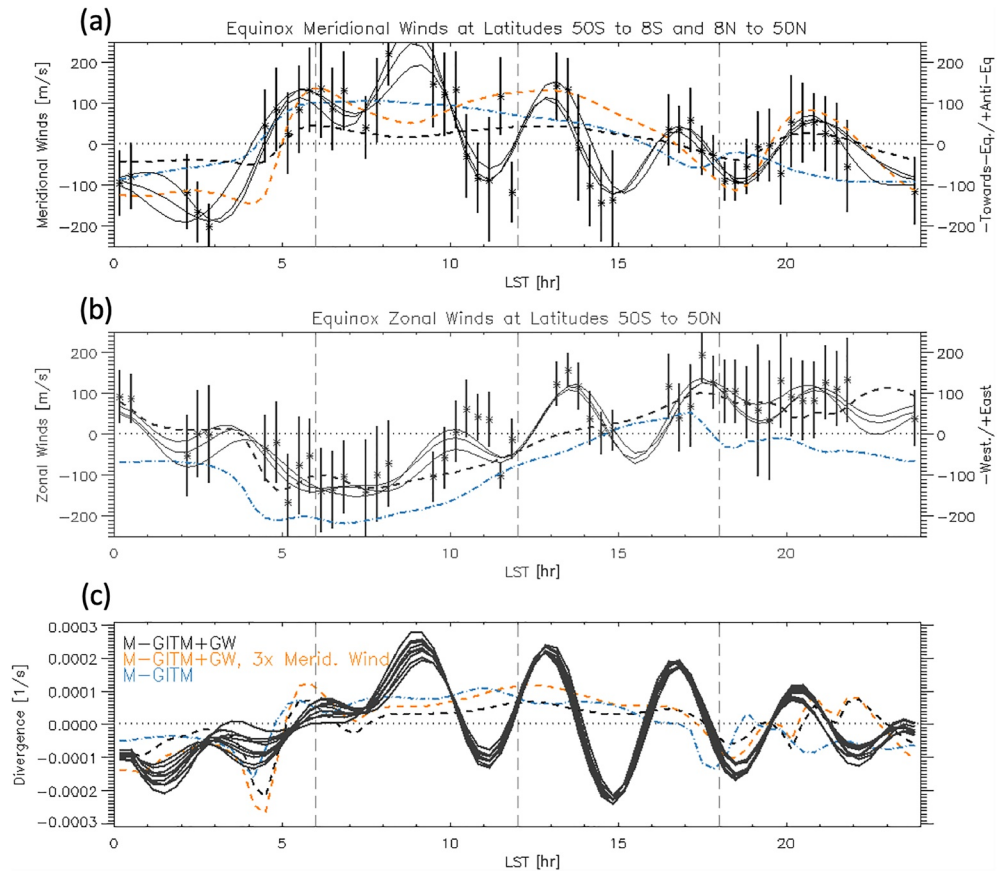
Figure 5. Equinox mid-latitude meridional winds (a), zonal winds (b), and divergence (c) based on the meridional and zonal fits. Dashed lines represent M-GITM model results and solid lines represent fits to the data. The various fits shown represent the uncertainty in the fitting results.

the standard M-GITM results (4b). Instead the afternoon winds in the M-GITM$_{GW}$ case continue in an eastward direction past midnight until 2–3 LST, resulting in enhanced convergence at these locations and better agreement with the statistical results. Overall wind magnitudes are reduced in M-GITM$_{GW}$, as are the model divergence values in panel 4f. Note that neither the standard M-GITM (4c) nor M-GITM$_{GW}$ (4f) manifest a dayside low/mid latitude convergence observed near 15 LST.

In order to further examine the low latitude divergence, we divide the low/mid-latitude wind data into 1/3 LST bins and combine meridional wind data between 8° and 50° MSO latitude and zonal data between 0° and 50° MSO latitude. The exclusion of lowest latitude meridional data is done to avoid the near zero meridional components near the equator (see Figure 4a). This way, the average meridional component (equatorward/anti-equatorward) is captured and can be used to compute a horizontal divergence assuming that the meridional winds reach zero by 0° latitude. A series of Fourier fits to the meridional and zonal components is then performed. The fits are based on average, upper, and lower quartile winds within each bin. The results are shown in Figures 5a and 5b for the meridional and zonal directions respectively.

Examining the peaks in equatorward (negative) winds in Figure 5a confirms some of the previous results but with a higher resolution and indicates that equatorward winds lead to convergence post-midnight (2–3 LST), near 15 LST, and near the dusk terminator. There is also a region of moderately equatorward winds at around 11 LST which was not apparent in the previous analysis but which seems to form part of a wave pattern that extends from approximately 10 LST to midnight. The associated wavelength is approximately 4 hr LST (3,500 km). Model meridional winds are shown for M-GITM (dashed blue line), M-GITM$_{GW}$ (dashed black), and M-GIT-M$_{GW}$ (dashed orange), where the meridional component is multiplied by a factor of three. Reasonable agreement between statistical and modeled meridional components is obtained when the model meridional component is significantly increased and when gravity waves are included (dashed orange).

The zonal winds in Figure 5b indicate convergence during east-to-west transitions (positive to negative) seen post-midnight, around 4 LST, 10–11 LST, and 14–15 LST. The zonal convergence locations are thus mostly consistent with the convergence of the meridional component. A wave pattern with an approximately 4-hr wavelength is also observed in the zonal measurements. The modeled zonal component is in general agreement with the statistical winds only when GW parametrization is included (black dashed line).

Combining the spatial derivatives from all six of the Fourier fits (three for each component) results in nine divergence estimates plotted in Figure 5c using solid lines. The dashed lines in panel 5c are the equinox M-GITM divergence values computed using the same sampling method as used to analyze the observed winds. The three largest statistical convergence values occur post-midnight (1–2 LST), near 15 LST, and near the dusk terminator (18–19 LST). The largest low-latitude M-GITM convergence values are seen at 4 LST, and the dusk terminator (18 LST). A large oscillation with a 4-hr wavelength appears in the statistical divergence estimates (solid black lines).

The dashed black lines in Figure 5 representing M-GITM$_{GW}$ results are in better overall agreement with the observed winds than the non-GW version of the model. A reference dashed orange line is simply the meridional winds output by M-GITM$_{GW}$ multiplied by a factor of three in the top panel. In the bottom panel, this orange dashed line represents the divergence calculation using this artificially tripled meridional wind. Note that the model was not altered to produce this new meridional value, only the output. Using the tripled magnitude of the meridional component improves data-model agreement in convergence further in the post-midnight and post-dusk regions (5a and 5c). The inclusion of GW parametrization significantly improves the zonal wind agreement between model and data, as seen in Figure 5b. As noted before, this places the night-time zonal wind reversal in the morning sector. Both the diurnal structure and magnitude of the M-GTIM$_{GW}$ zonal wind components agrees well with the data. Horizontal divergence comparisons were shown in Figure 5c. Two versions of M-GITM$_{GW}$ divergence were included, those with the original modeled wind magnitudes (black dashed line) and a version where the meridional wind magnitudes have been increased (orange dashed line). Night-time convergence peaks appear at 1–2 LST, 4–5 LST, 18–19 LST in the statistical analysis as well as M-GITM$_{GW}$. A smaller convergence observed near 22–23 LST is not seen in M-GITM$_{GW}$ although this feature may be a processing artifact resulting from the data gap between 22 and 24 LST. In the dayside, the appearance of an oscillation with a ∼4-hr wavelength can be seen in both data and M-GITM$_{GW}$ and, compared to the standard M-GITM results in panel 5c, the phase of the oscillation matches the observed divergence more closely. As with the standard M-GITM model, the amplitude of the M-GITM$_{GW}$ convergence oscillation is much smaller than that based on the Fourier expansion fits.

Figure 6 contains the constant-pressure empirical reconstruction of NGIMS derived temperatures and pressure-level heights that were described in Section 3.1 (panels a, b, e, f). The pressure-level values are 5.4×10^{-6} Pa (dashed), 1.3×10^{-6} Pa (solid), and 3.4×10^{-7} Pa (dotted). These results were evaluated for a constant EUV Lyman-alpha irradiance of 0.0032 Wm^{-2} and a range of latitudes between $\pm 50°$ MSO. The corresponding M-GITM results appear in panels c, d, g, and h for a range of latitudes between $\pm 30°$ MSO. The empirical reconstructions based on linear fits to EUV irradiance are shown in panels a and e, while those using non-linear fitting are shown in panels b and f. Figure 6 also contains estimated dynamical heating based on horizontal terms A and B in Equation 5 (panels i and j) and computed using the fits to the zonal and meridional wind observations shown in Figure 5. Note that panels i and j are identical and included for ease of comparison with the above panels. The modeled dynamical heating (based on all terms in Equation 5) is shown in red in panels k and j, along with the sum of the non-dynamical heating terms shown in black. Model results are included for the standard M-GITM runs in panels c, g, and k and for the M-GITM$_{GW}$ runs in panels d, h, l. In all panels, results are shown for three pressure levels indicated by the dotted, solid, and dashed lines. The pressure levels are separated from each other by a pressure factor of approximately four. The mean altitude of these pressure levels is shown in panels e, f, g, and h for the linear empirical reconstruction, non-linear reconstruction, standard M-GITM, and M-GITM$_{GW}$, respectively.

First considering the empirical temperature reconstructions in panels a and b, we observe a dayside peak temperature of ∼250 K near 12–15 LST and a nightside low temperature of 140–150 K around 20–24 LST. As the thermosphere rotates further away from the dayside, we would expect radiative cooling to result in ever decreased temperatures further from the dusk terminator. However, the reconstructed post-midnight temperatures (0–4 LST) are actually warmer than those before it. There are local temperature enhancements between 1 and 4 LST as well as 16–18 LST in both the linear (a) and non-linear (b) empirical reconstructions. A smaller temperature peak is
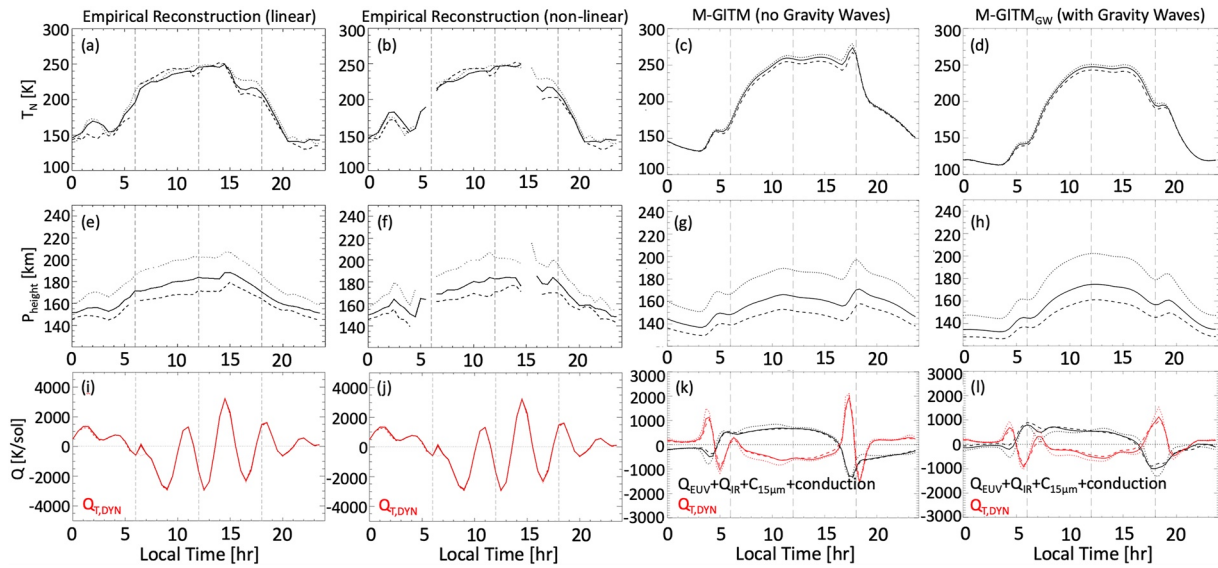
Figure 6. Climatological thermospheric temperatures at three constant pressure levels (a, b, c, d) and the corresponding pressure level heights (e, f, g, h) at equinox, low-to-mid latitudes (±50° MSO). The pressure-level values are 5.4×10^{-6} Pa (dashed), 1.3×10^{-6} Pa (solid), and 3.4×10^{-7} Pa (dotted). Dynamical heating terms are shown in panels (i, j, k, l). Panels (a, e, i) are an empirical reconstruction based on a linear response to EUV irradiance, panels (b, f, j) are an empirical reconstruction based on a nonlinear response for pressure-level heights only. Panels (c, g, k) are the M-GITM extracted at the equivalent conditions while panels (d, h, l) are equivalent M-GITM results for a model version that includes gravity wave effects.

present at 14–15 LST in panel (a) and corresponds to a peak in pressure-level altitudes at the same location (panel e). These heating and pressure-level uplift features correlate with the largest enhancements in observed dynamical heating at 1–4 LST, 13–16 LST, and 17–19 LST. The morning pressure enhancement, when interpreted at a fixed altitude between 150 and 160 km, results in an approximately 4x increase in pressure between 0 LST and 2–3 LST. In the linear analysis (see panel e), the 150 km pressure level begins at 1.3×10^{-6} Pa (solid line) at 0 LST and increases to nearly the 5.4×10^{-6} Pa pressure level (dashed line) by 2 LST. Meanwhile, the non-linear analysis (panel f) indicates an increase from 1.3×10^{-6} Pa (solid line) at 0 LST and 150 km to a pressure value exceeding the 5.4×10^{-6} Pa dashed line between 2 and 3 LST at the same altitude. Note that dynamical heating is present throughout the low-latitude morning region and is larger than the dynamical heating in the pre-midnight sector (panel i/j). This may explain why the morning (post-midnight) nighttime thermosphere in panels (a) and (b) is warmer than the pre-midnight thermosphere. A dip in temperatures near 11–12 LST and 16–17 LST seen in panels a and b correlates with the dynamical cooling (negative values) seen in panels i and j near the same locations. Taken together, these observed temperature decreases and enhancements follow the dynamical heating estimated from observed wind statistics and constitute an oscillation with an approximately 4-hr LST period.

Turning now to the model results, the empirical temperatures in panels a and b are best matched in terms of day-night ratio by the standard M-GITM run in panel c, which has dayside temperatures of ~250 K at 12–15 LST and 140–150 K around 20–24 LST. The location of the modeled dusk dynamical heating feature at 17–18 LST in panel c also agrees with the empirical results but its model amplitude is much higher. Meanwhile, the M-GITM$_{GW}$ temperatures in panel (d) have a larger diurnal amplitude (day-night ratio) and lower overall values than those observed with the dayside peak near ~240 K and the nightside lows of ~120 K. The dynamical heating temperature enhancement near dusk in M-GITM$_{GW}$ results occurs at a later local time (19 LST) but has a smaller amplitude that better matches the empirical temperature enhancement (~10 K increase). Another feature of the M-GITM$_{GW}$ temperature results (panel d) is a ~10 K peak near midnight that is absent in the standard M-GITM temperatures (panel c). This enhancement may correspond to the post-midnight temperature increase seen in the data (panels a and b at 1–4 LST). The modeled morning temperature enhancement near 5 LST appears in both model versions and is accompanied by an increase in modeled pressure-level height (panels g and h). A similar feature is difficult to identify in the empirical reconstructions of both temperature and pressure-level height. Qualitatively, the inclusion of GW parametrization improves the temperature structure associated with dynamical heating in the morning and dusk regions by broadening and attenuating the dynamical heating peaks (red lines in panel k compared to panel l). Both the dawn and dusk enhancements in modeled temperature and pressure-level

height correspond to the dynamical heating enhancements in panels k and l. The dampening of meridional winds by a factor of ~3 in the M-GITM$_{GW}$ relative to the wind statistics (Figure 5a) may be responsible for the reduction of night-time dynamical heating leading to the cooler morning temperatures in this version of the model.

6. Discussion

The MAVEN data analyzed here suggest thermospheric enhancements in neutral temperature at a fixed pressure level that corresponds to statistical wind convergence and dynamical heating. The most robust signal associated with dynamical heating seems to be responsible for enhanced temperatures in the deep night-side of the thermosphere. Additional evidence of dynamical heating appears near the dusk terminator and in the afternoon region. Both data and model suggest that the dynamical heating terms significantly modulate the overall thermal structure by modifying the overall heat balance between EUV heating, IR heating, 15 µm cooling, and conduction (responsible primarily for cooling). The global variation seen in the model dynamical heating causes corresponding temperature fluctuations in the model at fixed pressure. A similar dynamical heating oscillation is seen in the empirical reconstruction, especially in the dayside between 10 and 18 LST but has a much larger amplitude than either of the model versions evaluated here.

An important question is how the large amplitude dayside oscillation in divergence and the resulting oscillation in dynamical heating is generated. One of the surprising results of this analysis is that the observed dayside divergence pattern is responsible for dynamical heating near 15 LST, very close to the subsolar point. The increase in dynamical heating at this location is associated with a small enhancement in temperature as well as a significant increase in pressure-level height. It is possible that the presence of a smaller oscillation in the dayside model thermosphere (M-GITM and M-GITM$_{GW}$) provides a clue. The phase and wavelength of the observed modulation in dynamical heating/cooling signatures are better reproduced when GW parametrization is included in the model. However, the inclusion of GW parametrization results in modeled meridional wind components that are smaller than those observed at equinox. It is possible that the GW drag in the M-GITM model could be overestimated for this season, resulting in a meridional flow that is over-damped. This model-data comparison highlights the important coupling between GW effects, the global circulation pattern, and the resulting dynamical effects seen throughout the Martian thermosphere.

One possible explanation for the global-scale temperature, pressure, and wind-field oscillation is a terminator wave which propagates through the density and wind field. Simulations by Forbes and Moudden (2009) have shown that such a wave is possible and that it results in a density oscillation with a wavelength of ~2–4 hr LST (3,800–3,600 km), similar to that observed. Furthermore, extrapolating the density profile modeled by Forbes and Moudden to ~200 km altitude does result in a density enhancement at 15 LST, which is in qualitative agreement with the empirical results presented here as well as with the temperature structure in M-GITM$_{GW}$.

An alternative perspective is the presence of two, ~2,500 km diameter, dayside circulation cells at low to mid latitudes originating from solar heating and rapidly turning eastward then equatorward, leading to convergence around 15 LST. It is possible that these cells are mostly independent of any wave originating from the dusk terminator. The modeled (with or without GW parametrization) circulation patterns are much larger than this (>10,000 km diameter) with circulation diverging from the dayside mid-high latitudes and converging on the nightside. This difference might be explained by excessive modeled wind drag in the meridional direction, impeding the generation of smaller circulation cells. Whether or not this is the case could be tested in future studies. The smaller meridional wind magnitudes in the model are clearly visible in Figure 4a, especially in the night and terminator regions. A difference in meridional and zonal wave drag may stem from anisotropy in GW propagation at the source (~9 km altitude) or from anisotropic filtering of GW's below the thermosphere that is not represented in M-GITM$_{GW}$. Any modeled errors in lower-altitude (10–150 km) wind fields might also be manifested in the wind drag distribution.

7. Conclusions

Dynamical heating is critical to describing the large-scale structure of the Mars thermosphere. The presence of temperature and density features in the Martian thermosphere resulting from dynamical heating has been suggested previously by global circulation models such as M-GITM. The most prominent of these features are broad temperature enhancements in regions of converging winds occurring near the dawn and dusk terminators.

In this study, we have compared these modeled features with empirical representations based on several Mars years of data. In addition to evaluating the temperature at a fixed pressure, we have also looked at the observed thermospheric wind divergence at similar locations and conditions. In order to take advantage of the most complete empirical data set, the study focuses on the equinox seasons. The results indicate that dynamical heating predicted by models is indeed observed. The inclusion of GW parametrization in M-GITM generally improves the data-model agreement indicating that GW drag is critical in modulating the observed global circulation and the resulting thermospheric horizontal structure. The comparisons between M-GITM$_{GW}$ and the observations are not perfect, however, and work remains to be done to investigate the differences in wind patterns between the model and observations.

At equinox the most robust thermal features appear in the near-equatorial thermosphere in the post-midnight and near-dusk regions with the post-midnight enhancement having the larger relative amplitude. The M-GITM$_{GW}$ model contains analogous features near the dusk terminator as well as near midnight although the locations of these features are different by 1 or 2 hr of local time. The post-midnight feature somewhat resembles the midnight temperature maximum in the Earth's thermosphere (Akmaev et al., 2009) as well as the midnight temperature enhancement at Venus (Brecht et al., 2011). The former is likely a result of wave interactions and propagation from the lower atmosphere while the latter is associated with dynamical heating. Our analysis indicates that the midnight feature at Mars is a result of converging winds though some contribution from wave interactions cannot be excluded at this time. The appearance of a dayside convergence location and a corresponding pressure height and (subtle) temperature response was unexpected. The fact that this feature may be a part of a larger oscillation in the diurnal structure appearing across most of the Martian thermosphere is also a new result. M-GITM$_{GW}$ does contain a dynamical heating modulation with a peak at the same location (15 LST) and a corresponding broad feature in the dayside temperature. However, the modeled heating and the wind divergence pattern that causes it is much less pronounced. More observations are needed to ensure that this dayside equinox feature is not the result of sampling or aliasing of other effects. This is especially true of the surprising planetary scale oscillation found in the horizontal wind observations. Future analyses would benefit tremendously from continuous and dedicated wind observations to better understand this feature.

Data Availability Statement

The MAVEN/NGIMS number densities used in this study are the Level 2, version 8, release 2 data. The neutral winds were also collected by the NGIMS instrument and are the Level 3, version 3, release 1 data product. Both MAVEN/NGIMS data products are available on NASA's Planetary Data System (Benna & Lyness, 2015).

Solar fluxes used in the analysis are from the L2b orbit-averaged product from the MAVEN/EUVM instrument. The solar fluxes used to drive the M-GITM model are from the MAVEN/EUVM FISM-M empirical model and are a Level 3, Version 14, Revision 3 data product. Both MAVEN/EUVM data products are hosted on the Planetary Data System (Eparvier, 2017, 2022).

M-GITM model runs used in this work can be retrieved at the University of Michigan Deep Blue repository (Bougher & Pilinski, 2022).

References

Akmaev, R. A., Wu, F., Fuller-Rowell, T. J., & Wang, H. (2009). Midnight temperature maximum (MTM) in Whole Atmosphere Model (WAM) simulations. *Geophysical Research Letters*, *36*(7), L07108. https://doi.org/10.1029/2009GL037759

Benna, M., Bougher, S. W., Lee, Y., Roeten, K. J., Yiğit, E., Mahaffy, P. R., & Jakosky, B. M. (2019). Global circulation of Mars' upper atmosphere. *Science*, *366*(6471), 1363–1366. https://doi.org/10.1126/science.aax1553

Benna, M., & Lyness, E. (2015). MAVEN neutral gas and ion mass spectrometer data. [Dataset]. NASA Planetary Data System. https://doi.org/10.17189/1518931

Bougher, S., Jakosky, B., Halekas, J., Grebowsky, J., Luhmann, J., Mahaffy, P., et al. (2015). Early MAVEN Deep Dip campaign reveals thermosphere and ionosphere variability. *Science*, *350*(6261). https://doi.org/10.1126/science.aad0459

Bougher, S., & Pilinski, M. (2022). Dynamical heating in the Martian thermosphere. [Dataset]. University of Michigan - Deep Blue Data. https://doi.org/10.7302/t6gg-3t89

Bougher, S. W., Blelly, P.-L., Combi, M., Fox, J. L., Mueller-Wodarg, I., Ridley, A., & Roble, R. G. (2008). Neutral upper atmosphere and ionosphere modeling. *Space Science Reviews*, *139*(1–4), 107–141. https://doi.org/10.1007/s11214-008-9401-9

Bougher, S. W., Brain, D. A., Fox, J. L., Francisco, G.-G., Simon-Wedlund, C., & Withers, P. G. (2017). Upper neutral atmosphere and ionosphere. In *The atmosphere and climate of Mars* (pp. 433–463). Cambridge University Press. https://doi.org/10.1017/9781139060172.014

Bougher, S. W., Cravens, T. E., Grebowsky, J., & Luhmann, J. (2015). The Aeronomy of Mars: Characterization by MAVEN of the upper atmosphere reservoir that regulates volatile escape. *Space Science Reviews*, *195*(1–4), 423–456. https://doi.org/10.1007/s11214-014-0053-7

Bougher, S. W., Pawlowski, D., Bell, J. M., Nelli, S., McDunn, T., Murphy, J. R., et al. (2015c). Mars Global Ionosphere-Thermosphere Model: Solar cycle, seasonal, and diurnal variations of the Mars upper atmosphere. *Journal of Geophysical Research: Planets*, *120*(2), 311–342. https://doi.org/10.1002/2014JE004715

Bougher, S. W., Roble, R. G., Ridley, E. C., & Dickinson, R. E. (1990). The Mars thermosphere: 2. General circulation with coupled dynamics and composition. *Journal of Geophysical Research*, *95*(B9), 14811. https://doi.org/10.1029/JB095iB09p14811

Bougher, S. W., Roeten, K. J., Olsen, K., Mahaffy, P. R., Benna, M., Elrod, M., et al. (2017b). The structure and variability of Mars dayside thermosphere from MAVEN NGIMS and IUVS measurements: Seasonal and solar activity trends in scale heights and temperatures. *Journal of Geophysical Research: Space Physics*, *122*(1), 1296–1313. https://doi.org/10.1002/2016JA023454

Brecht, A. S., Bougher, S. W., Gérard, J.-C., Parkinson, C. D., Rafkin, S., & Foster, B. (2011). Understanding the variability of nightside temperatures, NO UV and O_2 IR nightglow emissions in the Venus upper atmosphere. *Journal of Geophysical Research*, *116*(E8), E08004. https://doi.org/10.1029/2010JE003770

Creasey, J. E., Forbes, J. M., & Keating, G. M. (2006). Density variability at scales typical of gravity waves observed in Mars' thermosphere by the MGS accelerometer. *Geophysical Research Letters*, *33*(22), L22814. https://doi.org/10.1029/2006GL027583

Crowley, G., Schoendorf, J., Roble, R. G., & Marcos, F. A. (1995). Satellite observations of neutral density cells in the lower thermosphere at high latitudes (pp. 339–348). https://doi.org/10.1029/GM087p0339

Deng, Y., Richmond, A. D., Ridley, A. J., & Liu, H.-L. (2008). Assessment of the non-hydrostatic effect on the upper atmosphere using a general circulation model (GCM). *Geophysical Research Letters*, *35*(1), L01104. https://doi.org/10.1029/2007GL032182

England, S. L., Liu, G., Yiğit, E., Mahaffy, P. R., Elrod, M., Benna, M., et al. (2017). MAVEN NGIMS observations of atmospheric gravity waves in the Martian thermosphere. *Journal of Geophysical Research: Space Physics*, *122*(2), 2310–2335. https://doi.org/10.1002/2016JA023475

Eparvier, F. (2017). MAVEN EUV bundle. [Dataset]. NASA Planetary Data System. https://doi.org/10.17189/1414171

Eparvier, F. (2022). MAVEN EUV modeled data bundle. [Dataset]. NASA Planetary Data System. https://doi.org/10.17189/1517691

Eparvier, F. G., Chamberlin, P. C., Woods, T. N., & Thiemann, E. M. B. (2015). The solar extreme ultraviolet monitor for MAVEN. *Space Science Reviews*, *195*(1–4), 293–301. https://doi.org/10.1007/s11214-015-0195-2

Forbes, J. M., & Moudden, Y. (2009). Solar terminator wave in a Mars general circulation model. *Geophysical Research Letters*, *36*(17), L17201. https://doi.org/10.1029/2009GL039528

González-Galindo, F., Bougher, S. W., López-Valverde, M. A., Forget, F., & Murphy, J. (2010). Thermal and wind structure of the Martian thermosphere as given by two General Circulation Models. *Planetary and Space Science*, *58*(14–15), 1832–1849. https://doi.org/10.1016/j.pss.2010.08.013

González-Galindo, F., Chaufray, J.-Y., López-Valverde, M. A., Gilli, G., Forget, F., Leblanc, F., et al. (2013). Three-dimensional Martian ionosphere model: I. The photochemical ionosphere below 180 km. *Journal of Geophysical Research: Planets*, *118*(10), 2105–2123. https://doi.org/10.1002/jgre.20150

Haberle, R. M., Joshi, M. M., Murphy, J. R., Barnes, J. R., Schofield, J. T., Wilson, G., et al. (1999). General circulation model simulations of the Mars Pathfinder atmospheric structure investigation/meteorology data. *Journal of Geophysical Research*, *104*(E4), 8957–8974. https://doi.org/10.1029/1998JE900040

Haberle, R. M., Murphy, J. R., & Schaeffer, J. (2003). Orbital change experiments with a Mars general circulation model. *Icarus*, *161*(1), 66–89. https://doi.org/10.1016/S0019-1035(02)00017-9

Hines, C. O. (1965). Dynamical heating of the upper atmosphere. *Journal of Geophysical Research*, *70*(1), 177–183. https://doi.org/10.1029/JZ070i001p00177

Jakosky, B. M., Lin, R. P., Grebowsky, J. M., Luhmann, J. G., Mitchell, D. F., Beutelschies, G., et al. (2015). The Mars Atmosphere and Volatile Evolution (MAVEN) mission. *Space Science Reviews*, *195*(1–4), 3–48. https://doi.org/10.1007/s11214-015-0139-x

Mahaffy, P. R., Benna, M., King, T., Harpold, D. N., Arvey, R., Barciniak, M., et al. (2015). The neutral gas and ion mass spectrometer on the Mars atmosphere and volatile evolution mission. *Space Science Reviews*, *195*(1–4), 49–73. https://doi.org/10.1007/s11214-014-0091-1

Medvedev, A. S., González-Galindo, F., Yiğit, E., Feofilov, A. G., Forget, F., & Hartogh, P. (2015). Cooling of the Martian thermosphere by CO_2 radiation and gravity waves: An intercomparison study with two general circulation models. *Journal of Geophysical Research: Planets*, *120*(5), 913–927. https://doi.org/10.1002/2015JE004802

Medvedev, A. S., & Yiğit, E. (2012). Thermal effects of internal gravity waves in the Martian upper atmosphere. *Geophysical Research Letters*, *39*(5). https://doi.org/10.1029/2012GL050852

Medvedev, A. S., Yiğit, E., & Hartogh, P. (2011). Estimates of gravity wave drag on Mars: Indication of a possible lower thermospheric wind reversal. *Icarus*, *211*(1), 909–912. https://doi.org/10.1016/j.icarus.2010.10.013

Pilinski, M., Bougher, S., Greer, K., Thiemann, E., Andersson, L., Benna, M., & Elrod, M. (2018). First evidence of persistent nighttime temperature structures in the neutral thermosphere of Mars. *Geophysical Research Letters*, *45*(17), 8819–8825. https://doi.org/10.1029/2018GL078761

Ridley, A. J., Deng, Y., & Tóth, G. (2006). The global ionosphere–thermosphere model. *Journal of Atmospheric and Solar-Terrestrial Physics*, *68*(8), 839–864. https://doi.org/10.1016/j.jastp.2006.01.008

Roeten, K. J., Bougher, S. W., Benna, M., Elrod, M., Medvedev, A., & Yigit, E. (2022). Impacts of gravity waves in the Martian thermosphere using M-GITM coupled with a whole atmosphere gravity wave scheme. *Journal of Geophysical Research: Planets*, *127*(12). https://doi.org/10.1029/2022JE007477

Schoendorf, J., Crowley, G., & Roble, R. G. (1996). Neutral density cells in the high latitude thermosphere—2. Mechanisms. *Journal of Atmospheric and Terrestrial Physics*, *58*(15), 1769–1781. https://doi.org/10.1016/0021-9169(95)00166-2

Siddle, A. G., Mueller-Wodarg, I. C. F., Stone, S. W., & Yelle, R. V. (2019). Global characteristics of gravity waves in the upper atmosphere of Mars as measured by MAVEN/NGIMS. *Icarus*, *333*, 12–21. https://doi.org/10.1016/j.icarus.2019.05.021

Smith, M. D. (2004). Interannual variability in TES atmospheric observations of Mars during 1999–2003. *Icarus*, *167*(1), 148–165. https://doi.org/10.1016/j.icarus.2003.09.010

Smith, M. D. (2009). THEMIS observations of Mars aerosol optical depth from 2002–2008. *Icarus*, *202*(2), 444–452. https://doi.org/10.1016/j.icarus.2009.03.027

Snowden, D., Yelle, R. V., Cui, J., Wahlund, J.-E., Edberg, N. J. T., & Ågren, K. (2013). The thermal structure of Titan's upper atmosphere, I: Temperature profiles from Cassini INMS observations. *Icarus*, *226*(1), 552–582. https://doi.org/10.1016/j.icarus.2013.06.006

Stone, S. W., Yelle, R. V., Benna, M., Elrod, M. K., & Mahaffy, P. R. (2018). Thermal structure of the Martian upper atmosphere from MAVEN NGIMS. *Journal of Geophysical Research: Planets*, *123*(11), 2842–2867. https://doi.org/10.1029/2018JE005559

Terada, N., Leblanc, F., Nakagawa, H., Medvedev, A. S., Yiğit, E., Kuroda, T., et al. (2017). Global distribution and parameter dependences of gravity wave activity in the Martian upper thermosphere derived from MAVEN/NGIMS observations. *Journal of Geophysical Research: Space Physics*, *122*(2), 2374–2397. https://doi.org/10.1002/2016JA023476

Thaller, S. A., Andersson, L., Thiemann, E., Pilinski, M. D., Fang, X., Elrod, M., et al. (2021). Martian nonmigrating atmospheric tides in the thermosphere and ionosphere at solar minimum. *Icarus*, *393*, 114767. https://doi.org/10.1016/j.icarus.2021.114767

Thiemann, E. M. B., Chamberlin, P. C., Eparvier, F. G., Templeman, B., Woods, T. N., Bougher, S. W., & Jakosky, B. M. (2017). The MAVEN EUVM model of solar spectral irradiance variability at Mars: Algorithms and results. *Journal of Geophysical Research: Space Physics*, *122*(3), 2748–2767. https://doi.org/10.1002/2016JA023512

Thiemann, E. M. B., Eparvier, F. G., Bougher, S. W., Dominique, M., Andersson, L., Girazian, Z., et al. (2018). Mars thermospheric variability revealed by MAVEN EUVM solar occultations: Structure at aphelion and perihelion, and response to EUV forcing. In arXiv.

Valeille, A., Combi, M. R., Bougher, S. W., Tenishev, V., & Nagy, A. F. (2009). Three-dimensional study of Mars upper thermosphere/ionosphere and hot oxygen corona: 2. Solar cycle, seasonal variations, and evolution over history. *Journal of Geophysical Research*, *114*(E11), E11006. https://doi.org/10.1029/2009JE003389

Yiğit, E., Aylward, A. D., & Medvedev, A. S. (2008). Parameterization of the effects of vertically propagating gravity waves for thermosphere general circulation models: Sensitivity study. *Journal of Geophysical Research*, *113*(D19), D19106. https://doi.org/10.1029/2008JD010135

Zurek, R. W., Tolson, R. A., Bougher, S. W., Lugo, R. A., Baird, D. T., Bell, J. M., & Jakosky, B. M. (2017). Mars thermosphere as seen in MAVEN accelerometer data. *Journal of Geophysical Research: Space Physics*, *122*(3), 3798–3814. https://doi.org/10.1002/2016JA023641